

## Effects of optically shallow bottoms on upwelling radiances: Bidirectional reflectance distribution function effects

Curtis D. Mobley<sup>1</sup>

Sequoia Scientific, Incorporated, Westpark Technical Center, 15317 Northeast 90th Street, Redmond, Washington 98052

Hao Zhang and Kenneth J. Voss

Department of Physics, University of Miami, Coral Gables, Florida 33124

### Abstract

Radiative transfer simulations were carried out for a variety of measured and modeled benthic bidirectional reflectance distribution functions (BRDFs), incident lighting conditions, bottom depths, and water inherent optical properties. These simulations quantify the errors that occur in predictions of above-surface remote-sensing reflectances and in-water upwelling radiances if non-Lambertian ocean bottoms are replaced by Lambertian bottoms having the same irradiance reflectance. We found that when computing water-leaving radiances, non-Lambertian BRDFs can be replaced by a Lambertian BRDF having the same irradiance reflectance, with errors seldom greater than 10% and often much less, for considerations of above-surface ocean-color remote sensing by Ocean Portable Hyperspectral Imager for Low-Light Spectroscopy (Ocean PHILLS) or similar systems using near-nadir viewing directions. The crucial measurement to make in characterizing the reflectance properties of a benthic surface for such applications is the spectral irradiance reflectance.

Optically shallow bottoms affect the reflected, upwelling radiance in various ways. The magnitude and angular distribution of the bottom-reflected radiance are determined by the bidirectional reflectance distribution function (BRDF) of the bottom. If the bottom is inhomogeneous, or patchy, the upwelling radiance is a spatial function of horizontal location as well as depth; the same is true if the bottom is not level. This paper considers BRDF effects for level, homogeneous bottoms. A companion paper (Mobley and Sundman 2003) considers the effects of patchy and sloping bottoms.

Consider a horizontal surface within a water body. This can be a physical surface such as the water–sand interface of a sandy bottom, or it can be simply a particular depth in the water column, e.g., 1 m above a seagrass bed or a given depth in optically deep water. In any case, we can think of light being incident onto the (real or conceptual) surface from all directions, with some of the incident light being reflected by the surface into all directions. To completely understand the optical properties of the surface, it is necessary to know how the surface reflects light going in any incident direction into any reflected direction. This information is given by the bidirectional reflectance distribution function (BRDF) of the surface.

To define the BRDF, let the reflecting surface lie in the  $x$ - $y$  plane of a Cartesian coordinate system whose  $z$  axis is

normal to the surface, as illustrated in Fig. 1. The light falling onto a surface is specified by the incident radiance  $L_i(\theta_i, \varphi_i)$ , where subscript  $i$  denotes incident,  $\theta$  is the polar angle measured from the normal to the surface, and  $\varphi$  is the azimuthal angle measured from the  $x$  axis, whose direction is chosen for convenience. For a given incident radiance having an element of solid angle  $d\Omega_i(\theta_i, \varphi_i)$ , let  $dL_r(\theta_r, \varphi_r)$  denote the radiance reflected (subscript  $r$ ) by the surface into direction  $(\theta_r, \varphi_r)$ . The BRDF is then defined as (Nicodemus et al. 1977; Modest 1993)

$$\text{BRDF}(\theta_i, \varphi_i, \theta_r, \varphi_r) \equiv \frac{dL_r(\theta_r, \varphi_r)}{L_i(\theta_i, \varphi_i) \cos \theta_i d\Omega_i(\theta_i, \varphi_i)} \quad (1)$$

Surface optical properties usually depend on the wavelength  $\lambda$ , so that the BRDF also depends on wavelength. We omit the  $\lambda$  in Eq. 1 for brevity. In the oceanographic setting of a horizontal bottom, the light incident onto the surface is traveling downward, and the light reflected by the surface is traveling upward. Thus, we will sometimes use subscript  $d$  for downward (incident) and  $u$  for upward (reflected) when necessary to conform to common oceanographic usage.

The BRDF has units of inverse steradians and can be interpreted as a reflectance per unit solid angle; it can have any nonnegative value. In Monte Carlo simulations, which trace individual photons, it is convenient to view the BRDF for a given incident photon direction  $(\theta_i, \varphi_i)$  as an (unnormalized) bivariate probability density function for the reflected angles  $\theta_r$  and  $\varphi_r$ .

The total radiance heading upward in direction  $(\theta_r, \varphi_r)$  owing to radiance incident onto the surface from all directions is obtained by solving Eq. 1 for  $dL_r(\theta_r, \varphi_r)$  and then integrating over all incident directions:

<sup>1</sup> Corresponding author (mobley@sequoiasci.com).

### Acknowledgments

This work was supported by the Environmental Optics Program of the United States Office of Naval Research under the Coastal Benthic Optical Properties research initiative. The authors thank Ronald Zaneveld and Emmanuel Boss for use of their ac-9 data and Charles Mazel for use of his bottom-reflectance data, and all three are thanked for their comments on the paper.

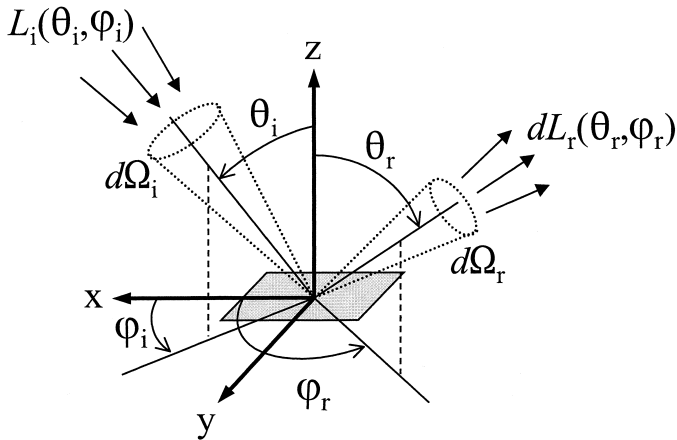


Fig. 1. Geometry used in the definition of the BRDF. The reflecting surface lies in the  $x$ - $y$  plane; the  $z$  axis is normal to the surface.

$$L_r(\theta_r, \varphi_r) = \int_{2\pi_i} L_i(\theta_i, \varphi_i) \text{BRDF}(\theta_i, \varphi_i, \theta_r, \varphi_r) \cos \theta_i d\Omega_i \quad (2)$$

Here  $2\pi_i$  denotes the set of all incident directions, which corresponds to a solid angle of  $2\pi$  sr. Integrals of this form are usually evaluated as double integrals in spherical coordinates, in which case  $d\Omega = \sin \theta d\theta d\varphi$ . Equation 2 shows the manner in which the BRDF is employed in the Hydro-light radiative transfer model (Mobley et al. 1993; Mobley 1994) to define the boundary condition for any type of bottom.

The irradiance reflectance of a surface is defined as

$$R = \frac{E_u}{E_d} = \frac{\int_{2\pi_r} L_r(\theta_r, \varphi_r) |\cos \theta_r| d\Omega_r}{\int_{2\pi_i} L_i(\theta_i, \varphi_i) |\cos \theta_i| d\Omega_i} \quad (3)$$

where the radiances are evaluated at the surface.  $E_u$  and  $E_d$  are the upwelling and downwelling plane irradiances, respectively. The reflectance properties of ocean bottoms are often specified by  $R(\lambda)$  as determined from spectral  $E_u(\lambda)$  and  $E_d(\lambda)$  measurements made as close to the bottom as possible. Substituting Eq. 2 into Eq. 3 gives

$$R = \left\{ \int_{2\pi_r} \left[ \int_{2\pi_i} L_i(\theta_i, \varphi_i) \text{BRDF}(\theta_i, \varphi_i, \theta_r, \varphi_r) |\cos \theta_i| d\Omega_i \right] \times |\cos \theta_r| d\Omega_r \right\} / \left( \int_{2\pi_i} L_i(\theta_i, \varphi_i) |\cos \theta_i| d\Omega_i \right) \quad (4)$$

Equation 4 is completely general and shows that the irradiance reflectance of a surface depends both on the surface itself, via the BRDF, and on the incident radiance. If the incident radiance is isotropic, Eq. 4 reduces to

$$A = \frac{1}{\pi} \int_{2\pi_r} \left[ \int_{2\pi_i} \text{BRDF}(\theta_i, \varphi_i, \theta_r, \varphi_r) |\cos \theta_i| d\Omega_i \right] |\cos \theta_r| d\Omega_r \quad (5)$$

$A$ , which is called the bihemispherical albedo, is often used as a convenient quantity for comparison of the total reflectances of various surfaces, even though incident radiances in nature are never isotropic.

Lambertian surfaces are idealized surfaces that by definition reflect light such that the measured reflected radiance is independent of viewing direction. If the incident irradiance onto the surface changes, the magnitude of the reflected radiance changes, but it remains directionally isotropic. However, all materials are, at least to some extent, non-Lambertian reflectors. The terrestrial remote-sensing community has made many measurements of, and developed models for, the non-Lambertian BRDFs of soils and plant canopies (e.g., Hapke 1993; Cabot and Dedieu 1997). The same has not been true in oceanography owing both to an historical research emphasis on optically deep waters and to the difficulties of making in-water measurements of BRDFs. The first in-water measurements of benthic BRDFs have been made only recently (Voss et al. 2000; Zhang et al. 2003). Owing both to the lack of measured or modeled BRDFs for benthic materials and to the extra computations required when using non-Lambertian BRDFs, oceanographers usually assume that benthic BRDFs are Lambertian (e.g., Gordon and Brown 1974; Lyzenga 1978; Philpot 1989; Maritorea et al. 1994; Lee et al. 1998). It is therefore necessary to quantify the errors induced by the assumption of Lambertian bottoms.

We first examine the extent to which the irradiance reflectance  $R$  of actual and hypothetical benthic BRDFs depends on the incident radiance for typical underwater light fields. We then quantify the errors that occur in predictions of above-surface remote-sensing reflectances and in-water upwelling radiances if non-Lambertian ocean bottoms are replaced by Lambertian bottoms having the same irradiance reflectance.

## BRDFs

We wish to study the effects of various possible benthic BRDFs on the upwelling radiance. We therefore select several BRDFs that may describe bare substrates such as sand or vegetation canopies such as sea grass.

*Lambertian surfaces*—As already noted, a Lambertian surface reflects radiance equally into all directions. Its BRDF is simply

$$\text{BRDF}_{\text{Lamb}}(\theta_i, \varphi_i, \theta_r, \varphi_r) = \frac{\rho}{\pi} \quad (6)$$

where  $\rho$  is called the reflectivity of the surface. The reflectivity varies from zero for a completely absorbing surface to one for a completely reflecting surface. Substituting Eq. 6 into Eqs. 4 and 5 shows that  $R = A = \rho$  for all incident radiances if (and only if) the BRDF is Lambertian. Thus a measurement of the irradiance reflectance completely spec-

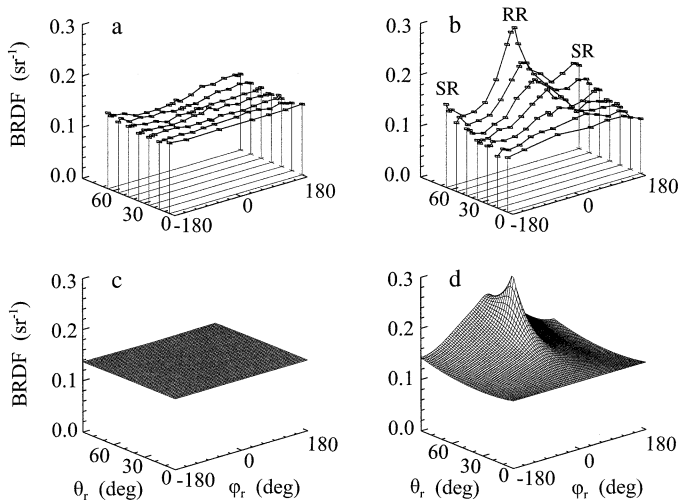


Fig. 2. Measured and modeled BRDF of ooid sand at a wavelength of 475 nm for two incident directions: (a) measured BRDF for  $(\theta_i, \varphi_i) = (0, 0)$ ; (b) measured for  $(\theta_i, \varphi_i) = (65, 0)$ ; (c) modeled BRDF corresponding to panel a; (d) modeled BRDF corresponding to panel b. In panel b, RR identifies the direction of retroreflection and SR identifies the direction of specular reflection.

ifies the reflectance properties of a Lambertian surface. Because of their simplicity, we use Lambertian surfaces as the standard against which to compare all non-Lambertian surfaces.

**Sediments**—The BRDFs of various sediments were measured in situ with diver-operated instruments during the Coastal Benthic Optical Properties (CoBOP) field experiments at Lee Stocking Island (LSI), Bahamas (Zhang et al. 2003). The sediments include bright, white ooid sand; yellow grapestone with a noticeable biofilm; and a bioturbated grapestone. These BRDFs were measured at nominal wavelengths of 475, 570, and 658 nm. The BRDFs were measured at discrete incident polar angles from 0 to 65°, at discrete reflected polar angles between 5 and 65°, and at discrete reflected azimuthal angles covering the full 360° range, for a total of about 100 reflected directions for a given incident direction.

Figure 2 shows an example of a measured and modeled BRDF of ooid sand at 475 nm for two incident angles. The incident azimuthal direction is chosen to be  $\varphi_i = 0$ . The plots show the full range of reflected directions;  $\varphi_r = 180$  and  $-180^\circ$  are the same direction. Panels a and b of the figure show the measured BRDF for incident polar angles of  $\theta_i = 0$  and 65°, respectively. The diamonds connected by the heavy lines indicate the discrete reflected directions at which the BRDF was measured for the given incident direction.

BRDFs of rough surfaces such as sand or vegetation canopies often show a “hot spot” or retroreflection. This phenomenon, caused by “shadow hiding” when the light source and observer are aligned, manifests itself as a peak in the BRDF at  $(\theta_r, \varphi_r) = (\theta_i, \varphi_i)$ . Smooth surfaces often show specular reflection at the angles where a mirror would reflect light:  $(\theta_r, \varphi_r) = (\theta_i, \varphi_i + 180^\circ)$ . The nearly constant BRDF

of Fig. 2a shows that the sand is well approximated as a Lambertian reflector for normally incident light. However, for incident polar angles greater than about 35°, the sand shows noticeable retroreflection. As seen in panel b, the BRDF increases by more than a factor of two near the retroreflection direction  $(\theta_r, \varphi_r) = (65, 0)$ , compared to the value at  $\theta_r = 0$ . There is a smaller increase in the BRDF near the specular direction  $(\theta_r, \varphi_r) = (65, \pm 180)$ . Thus the sand is a non-Lambertian reflector for incident angles  $\theta_i > 35^\circ$ . However, the symmetry in  $\varphi_r$  indicates that the sand BRDF is azimuthally symmetric to a good approximation. This means that the BRDF depends only on the difference in  $\varphi_i$  and  $\varphi_r$ , which allows for simpler analytical models of the BRDF and for simplifications in radiative transfer calculations.

The discrete data, shown in part in Fig. 2a and 2b, can be fit by an analytical function (Zhang et al. 2003) that differs from the measurements by less than 20%. Panels c and d of Fig. 2 show the analytic BRDFs corresponding to panels a and b, respectively. These functions extend the measurements over the entire range of incident and reflected angles, as is necessary for numerical modeling. The bihemispherical albedo of this BRDF, computed using the Zhang et al. analytic functions in Eq. 5, is  $A = 0.47$ . If the sand were Lambertian, the BRDFs seen in Fig. 2 would therefore have values of  $A/\pi = 0.15 \text{ sr}^{-1}$  for all  $(\theta_r, \varphi_r)$ .

**Vegetation canopies**—A number of models exist for the BRDFs of terrestrial plant canopies such as grasslands, crops, and forests; these models are reviewed in Cabot and Dedieu (1997). Canopy models typically have several free parameters whose values can be chosen to fit measured BRDFs of specific vegetation types. The BRDFs of aquatic vegetation canopies have yet to be measured. We therefore adopt the general canopy model of Rahman et al. (1993) as an ersatz aquatic vegetation BRDF. The Rahman et al. BRDF has three parameters:  $\rho_0$  sets the overall magnitude;  $k$  determines the extent to which the overall BRDF departs from Lambertian as a function of  $\theta_i$  and  $\theta_r$ ; and  $\Theta$  determines the contribution of the hot spot. Irradiance measurements made in situ just above dense sea grass canopies show that  $R$  lies in the range of 0.05 to 0.1 at blue and green wavelengths. In the simulations below, we therefore choose  $\rho_0$  values to give  $A = 0.1$ , which also gives  $R$  values in the observed range when the canopy is illuminated by typical underwater radiance distributions. For  $k$  and  $\Theta$  we use values determined from measured BRDFs of wheat or coniferous forest at visible wavelengths (Rahman et al. 1993, Table 1). We do not, of course, argue that sea grass BRDFs look like those of either wheat or conifers. These two terrestrial BRDFs were chosen because they differ greatly from Lambertian, and therefore may serve as worst-case BRDFs for benthic vegetation canopies, in the sense that the errors resulting from replacing these BRDFs with a Lambertian BRDF may be greater than the corresponding errors for actual benthic vegetation canopies. Benthic vegetation does not, for example, display any obvious hot spot or specular reflection when viewed underwater. Figure 3a,b shows these two BRDFs for incident polar angles of  $\theta_i = 30^\circ$ . The Rahman et al. model BRDFs become unbounded as  $\theta_i$  and  $\theta_r$  approach 90°. This

Table 1. Benthic BRDFs used in Hydrolight simulations.

BRDF	Label	Albedo, A
White ooid sand (475 nm)	Sand	0.47
Yellow grapestone (475 nm)	Grpst	0.11
Bioturbated grapestone (570 nm)	Turb	0.42
Wheat (visible wavelengths)	Wheat	0.10
Coniferous forest (visible wavelengths)	Conif	0.10
Closely packed anisotropically scattering particles	ASP	0.47

is a common feature of analytic BRDF models and is mathematically permissible because the BRDF is always multiplied by the cosine of these angles when used to compute reflectances, as seen in Eq. 4. The irradiance reflectance  $R$  is always bounded by 0 and 1.

*Other*—Figure 3c,d shows two other BRDFs that can be used as bottom boundaries in oceanic radiance simulations. Figure 3c shows a BRDF developed from radiative transfer theory (Hapke 1993, Eq. 8.89) for an infinitely deep layer of closely packed, anisotropically scattering particles. This BRDF contains four parameters ( $g = -0.1$ ,  $w = 0.88$ ,  $h = 0.1$ ,  $B_0 = 0.5$ ) whose values for Fig. 3c were chosen by trial and error to give a BRDF with the same  $A$  and overall shape as the measured sand BRDF of Fig. 2.

The BRDF of a homogeneous, infinitely deep body of water can be computed exactly given the total absorption and scattering coefficients and scattering phase function of the water (Mobley 1994, Eq. 9.76). BRDFs computed in this way are used in Hydrolight to simulate optically infinitely deep water below the maximum depth where output is desired. Figure 3d shows an example of such a BRDF as computed within Hydrolight for an infinitely deep layer of water whose absorption and scattering properties were defined from a biooptical model for case 1 water (as available in Hydrolight) with a chlorophyll concentration of  $1 \text{ mg m}^{-3}$

and a Petzold average-particle phase function for the particles. (The line spacing used to draw the figure corresponds to the  $\theta$ ,  $\varphi$  values used in Hydrolight.) Unlike the BRDFs of sand or vegetation, this BRDF shows no retroreflection or specular reflection, but it does show a maximum for reflection at horizontal directions ( $\theta_r = 90^\circ$ ). This is consistent with the observation that within deep waters the horizontal radiance is several times greater than the radiance seen looking straight down ( $\theta_r = 0$ ). We present this BRDF in Fig. 3 for the sake of comparison with those of physical benthic surfaces. We exclude it from our simulations below because it is not characteristic of benthic materials and, in any case, Hydrolight automatically incorporates the appropriate non-Lambertian BRDF when simulating infinitely deep water.

Table 1 lists the non-Lambertian benthic BRDFs used in the simulations below.

### BRDF effects on bottom reflectance

According to Eq. 4, the bottom irradiance reflectance  $R$  depends on the incident radiance if the bottom is non-Lambertian. For a given BRDF, the radiance incident onto the bottom changes with solar zenith angle, water inherent optical properties (IOPs), and bottom depth. We therefore first consider the extent to which  $R$  varies with these parameters for the BRDFs of Table 1.

We performed Hydrolight simulations for solar zenith angles (in air) of  $\theta_s = 0, 20, 40, 60$ , and  $88^\circ$  (sunrise/sunset). The corresponding range in incident angles  $\theta_i$  of the sun's direct beam onto the bottom, as refracted through a level sea surface, is  $0$  to  $48^\circ$ . The sky radiance incident onto the sea surface simulated a clear sky using the semianalytical sky radiance model of Harrison and Coombes (1988), which is available in Hydrolight. This sky radiance model includes the effects of surface-reflected radiance as backscattered by the atmosphere. The water surface was modeled with wave-slope statistics for a  $5 \text{ m s}^{-1}$  wind. The water IOPs were defined by the albedo of single scattering,  $\omega_0$ , and the scattering phase function. Two sets of water IOPs were simulated: (1) highly scattering water,  $\omega_0 = 0.85$ ; and (2) highly absorbing water,  $\omega_0 = 0.33$ . These values were based on absorption ( $a$ ) and scattering ( $b$ ) coefficients measured during the CoBOP field experiments at LSI, for which typical values are as follows:  $a = 0.05 \text{ m}^{-1}$  and  $b = 0.28 \text{ m}^{-1}$  at  $475 \text{ nm}$ , in which case  $\omega_0 = b/(a + b) = 0.85$ ;  $a = 0.4 \text{ m}^{-1}$  and  $b = 0.2 \text{ m}^{-1}$  at  $658 \text{ nm}$ , which give  $\omega_0 = 0.33$ . In each case the scattering phase function was taken to be the Petzold "average particle" phase function defined in Mobley et

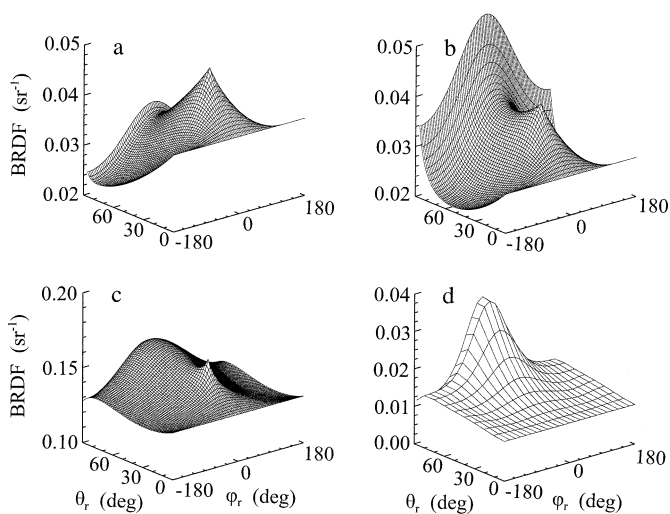


Fig. 3. Examples of BRDFs for an incident direction  $(\theta_i, \varphi_i) = (30, 0)$ : (a) wheat field; (b) coniferous forest; (c) anisotropically scattering particles; (d) infinitely deep, homogeneous water.

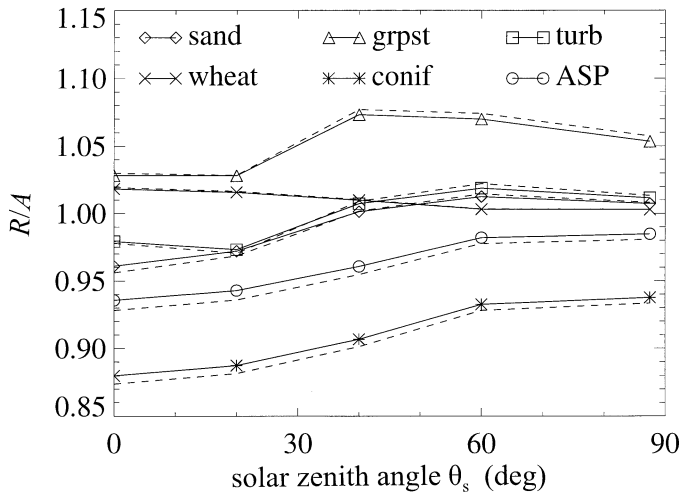


Fig. 4. Dependence of bottom irradiance reflectance on solar zenith angle for a bottom optical depth of 0.1. Each irradiance reflectance is normalized by the respective bihemispherical reflectance, shown in Table 1, which also identifies the various BRDFs. Solid lines are for highly scattering water,  $\omega_0 = 0.85$ , and dashed lines are for highly absorbing water,  $\omega_0 = 0.33$ .

al. (1993). Simulations were made with the bottom at optical depths of  $\zeta = 0.1, 1$ , and  $10$ , which correspond to optically very shallow to deep waters. For the typical LSI water, one optical depth,  $\zeta = (a + b)z$  in homogeneous water, corresponds to a physical depth of  $z = 3.0$  m for the highly scattering water at  $475$  nm, and to  $1.7$  m for the highly absorbing water at  $658$  nm. Hydrolight simulations were performed for these combinations of BRDF, solar angle, water IOPs, and bottom depths, for a total of 180 simulations.

Figure 4 shows the resulting values of  $R$  for a bottom depth of  $\zeta = 0.1$ ; the  $R$  values are normalized by the bihemispherical albedos  $A$  of the respective BRDFs, which are shown in Table 1. For all BRDFs except one, the value of  $R$  is within  $\pm 8\%$  of the respective  $A$  value for all solar angles, IOPs, and bottom depths; for the coniferous forest BRDF,  $R$  is as much as  $13\%$  less than  $A$ . For a given BRDF, the value of  $R$  never varies by more than  $6\%$  over the full range of solar angles. The water IOPs change  $R$  by less than  $1\%$  in all cases. Non-Lambertian effects are greatest for optically very shallow water, in which case the sun's direct beam dominates the radiance incident onto the bottom. As the bottom depth increases, scattering creates a more diffuse incident radiance.  $R$  then becomes closer to  $A$ , and the dependence of  $R$  on solar angle and IOPs becomes weaker. When  $\zeta = 10$ , the variability in  $R$  is less than  $3\%$  over all BRDFs, solar angles, and IOPs.

These simulations show that for the BRDFs considered here, the bottom irradiance reflectance for a given BRDF does not depend strongly on the solar angle, water IOPs, or bottom depth. In regard to the computation of bottom reflectance, these BRDFs behave as Lambertian surfaces to within errors of order  $10\%$ . This suggests that, for some purposes at least, it may be acceptable to replace a non-Lambertian bottom, whose reflectance is measured for particular lighting and water conditions, with a Lambertian bottom having the same  $R$  value. Note that the sun's direct beam

as refracted through a level surface, which dominates the incident radiance in shallow waters, is never incident onto the bottom at angles greater than  $48^\circ$ , for which the bottom BRDFs may be very non-Lambertian.

### BRDF effects on remote-sensing reflectance

The computation of  $R$  involves radiance in all directions—in particular, large incident angles  $\theta_i$  for which the BRDF may display significant retroreflection or specular reflection (recall Fig. 2) and large reflected angles  $\theta_r$  for which the BRDF may become large (recall Fig. 3). Thus  $R$  samples the BRDF over all directions and should be sensitive to non-Lambertian effects. However, most above-water, ocean-color remote sensing is done for a limited range of solar zenith angles and viewing directions. We therefore next consider BRDF effects on the water-leaving radiance, or equivalently on the remote-sensing reflectance, for the solar angles and viewing geometry relevant to remote sensing.

The Ocean Portable Hyperspectral Imager for Low-Light Spectroscopy (Ocean PHILLS; Davis et al. 2002) airborne ocean-color sensor was used extensively in the CoBOP field programs. To avoid sun glint, remote sensing with PHILLS is usually performed when the solar zenith angle is  $40$  to  $60^\circ$ , and PHILLS views the ocean at nadir angles from  $0$  to  $30^\circ$  and at an azimuthal angle nominally perpendicular to the sun's direction. A solar angle of  $60^\circ$  corresponds to an in-water incident angle of  $\sim 40^\circ$  for the sun's direct beam incident on the bottom (for a level sea surface and no scattering within the water), and an in-air nadir viewing angle of  $30^\circ$  corresponds to light reflected from the bottom at an in-water angle of  $\sim 22^\circ$ . Thus, the water-leaving radiance is affected by the BRDF over its full range of incident and reflected angles only to the extent that scattering within the water adds to the radiance of the unscattered direct solar beam as reflected by the bottom into the viewing direction. We therefore anticipate that the water-leaving radiance as relevant for PHILLS observations may be even less sensitive to non-Lambertian effects than is the bottom reflectance  $R$ . Sensors such as SeaWiFS use a larger, but still restricted, set of viewing directions.

Both the PHILLS and SeaWiFS sensors use the remote-sensing reflectance  $R_{rs}$ , deduced from the at-sensor radiance after atmospheric correction, as the basis for retrieval of water-column or bottom characteristics. The remote-sensing reflectance is defined as

$$R_{rs}(\theta_v, \varphi_v) \equiv \frac{L_w(\theta_v, \varphi_v)}{E_d}$$

Here  $L_w(\theta_v, \varphi_v)$  is the water-leaving radiance, i.e., the upwelling radiance just above the sea surface after removal of surface-reflected sky radiance, and  $E_d$  is the downwelling plane irradiance incident onto the sea surface. An in-air sensor viewing direction  $(\theta_v, \varphi_v)$  can be related to a bottom-reflectance direction  $(\theta_r, \varphi_r)$  via Snell's law for a level water surface. However, a given viewing direction will contain radiance reflected from the bottom into all directions, owing to scattering within the water column and to tilted wave facets at the surface.

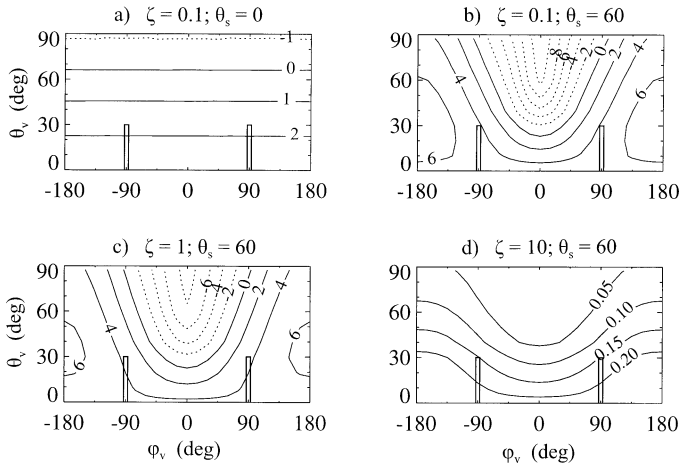


Fig. 5. Contours of the percentage error in the remote-sensing reflectance  $R_{rs}$  caused by replacing the non-Lambertian BRDF of Fig. 2 with a Lambertian BRDF having the same irradiance reflectance. Axes show the in-air viewing direction  $(\theta_v, \varphi_v)$ . Panels are labeled by the optical depth  $\zeta$  of the bottom and the solar zenith angle  $\theta_s$ . Solid lines are positive errors according to Eq. 7, i.e.,  $R_{rs}$  (Lambertian)  $>$   $R_{rs}$  (non-Lambertian). Dotted lines are negative errors.

To quantify the effects of non-Lambertian bottoms on  $R_{rs}$ , we performed Hydrolight simulations in which a non-Lambertian bottom was replaced by a Lambertian bottom having the same irradiance reflectance  $R$  for the given solar angle, water IOPs, and bottom depth. The percentage error in the predicted  $R_{rs}$  that would result from assuming the bottom to be Lambertian, when in reality it is non-Lambertian, is then

$$\text{Percent error in } R_{rs} = 100 \frac{R_{rs}(\text{Lambertian}) - R_{rs}(\text{non-Lambertian})}{R_{rs}(\text{non-Lambertian})} \quad (7)$$

Figure 5 shows contour plots of the percentage errors in  $R_{rs}$  that result from replacing the white sand BRDF of Fig. 2 by a Lambertian BRDF. The IOPs were for highly scattering water. Note that the axes are in-air viewing direction  $(\theta_v, \varphi_v)$ . The panels are labeled by bottom optical depth  $\zeta$  and solar angle (in air)  $\theta_s$ . The bars drawn at  $\varphi_v = \pm 90^\circ$  show the viewing angles relevant to the PHILLS sensor. The errors increase with increasing solar angle (panels a and b) and decrease with increasing depth (panels b–d). Even for the case of optically very shallow water and large solar angle, the error in  $R_{rs}$  is less than 5% for the viewing angles relevant to PHILLS.

Figure 6 shows corresponding contour plots for other BRDFs, for a depth of  $\zeta = 0.1$  and  $\theta_s = 60^\circ$ . For these BRDFs the maximum  $R_{rs}$  errors can be as large as  $\pm 25\%$ . The errors are large and negative near the retroreflection direction  $(\theta_v, \varphi_v) = (60, 0)$ , where the hot spot makes the non-Lambertian BRDF greater than its Lambertian replacement. However, over the range of viewing directions relevant to PHILLS remote sensing, the errors are in the  $-5$  to  $+10\%$  range. As in Fig. 5, these errors decrease with increasing depth or decreasing solar zenith angle.

Figure 7 gives another illustration of the bottom-related

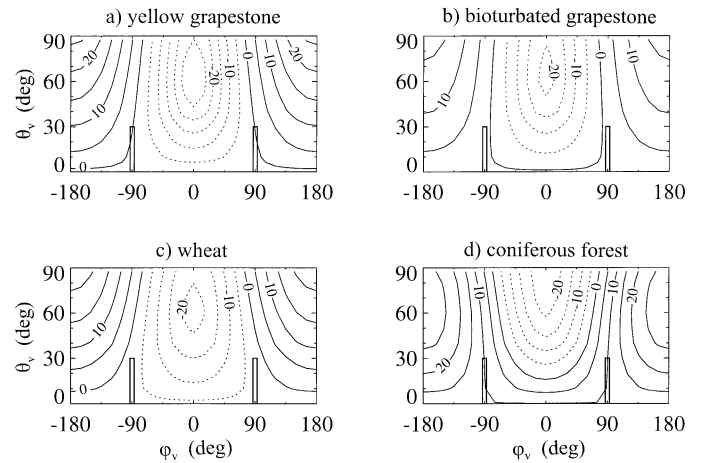


Fig. 6. Contours of the percentage error in the remote-sensing reflectance  $R_{rs}$  caused by replacing non-Lambertian BRDFs with Lambertian BRDFs having the same irradiance reflectance. Axes show the in-air viewing direction  $(\theta_v, \varphi_v)$ . Panels are labeled by the BRDF shown in Table 1. Each plot is for bottom optical depth  $\zeta = 0.1$  and solar zenith angle  $\theta_s = 60^\circ$ .

errors that can occur in  $R_{rs}$ . Simulations were performed for a water depth of 5 m. Water IOPs were obtained from WET-Labs ac-9 measurements made near LSI over a nominal wavelength range of 412 to 715 nm (the same data as used to define the  $\omega_0 = 0.33$  and  $0.85$  IOP cases discussed above). For these IOPs, 5 m corresponds to optical depths of 1.6 to 3.9, depending on wavelength. The sun was at a zenith angle of  $60^\circ$ . The plotted  $R_{rs}$  spectra are for a viewing direction of  $(\theta_v, \varphi_v) = (0, 0)$ , i.e., looking straight down. In panel a of the figure, the solid line shows  $R_{rs}(\lambda)$  computed using the angular pattern of the non-Lambertian ooid sand BRDF of Fig. 2, but with the magnitude of the BRDF adjusted at each wavelength  $\lambda$  to give a bottom reflectance  $R(\lambda)$  equal to the value shown by the dash-dot line and the right-side ordinate. This  $R(\lambda)$  spectrum was measured in situ by a diver-operated instrument (Mazel 1997). The dashed line shows  $R_{rs}$  as computed for a Lambertian bottom having the same  $R$ . Thus the difference in the solid and dashed lines shows the effect of replacing the non-Lambertian angular dependence with a

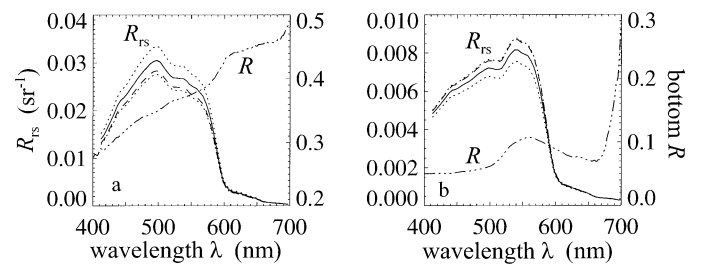


Fig. 7. Remote-sensing reflectances  $R_{rs}$  for (a) ooid sand and (b) sea grass bottoms at a water depth of 5 m.  $R_{rs}$  curves are coded as follows: solid lines, non-Lambertian BRDFs; dashed lines, Lambertian BRDFs having the same irradiance reflectance  $R$ ; dotted lines, non-Lambertian BRDFs with  $R$  values 1.1 and 0.9 times the  $R$  of the solid line. The dash-dot line and the right-hand ordinate show the  $R$  values corresponding to the solid lines.

Lambertian dependence, while still having the correct  $R$ . The dotted lines show  $R_{rs}$  as computed using the non-Lambertian angular dependence, but with the magnitude of the BRDF adjusted to give  $R$  values 1.1 (upper dotted line) and 0.9 (lower dotted line) times the measured  $R$  value at each wavelength. Comparison of the solid and dotted lines thus shows the errors in  $R_{rs}$  resulting from overestimating or underestimating the bottom reflectance by 10%, while still having the correct angular dependence of the BRDF. Panel b of Fig. 7 shows the corresponding curves for a sea grass bottom at 5 m. The bottom reflectance for sea grass was measured in situ above a dense sea grass bed.

In Fig. 7, the maximum error induced by replacing the non-Lambertian BRDFs with Lambertian BRDFs, computed via Eq. 7, is 7%. The corresponding errors for the other BRDFs of Table 1 also are never more than 7%. We thus see that, for the particular IOPs and solar zenith angle used to generate Fig. 7, replacing a non-Lambertian BRDF with a Lambertian BRDF having the same  $R$  value gives errors in  $R_{rs}$  that are somewhat less than the errors caused by a 10% error in the measurement of the overall magnitude of the non-Lambertian BRDF. These errors decrease with increasing water depth and decreasing solar zenith angle. For example, when the sun is at the zenith and the water depth is 5 m, the maximum error is 5%. Even for the extreme case of 1-m water depth and a 60° solar zenith angle, the maximum magnitude of the error is less than 11%, which is the same as the error caused by a 10% error in  $R$ .

### Measurement of $R$

We have seen that, in regard to computations of bottom reflectance or water-leaving radiance in directions relevant to PHILLS ocean-color remote sensing, the non-Lambertian BRDFs of Table 1 can be replaced by Lambertian BRDFs, with errors no more than 11% so long as the Lambertian BRDF has the same  $R$  as the original BRDF. If this level of accuracy is acceptable, then it is necessary to measure or model only the bottom irradiance reflectance  $R$ . The bottom BRDF then can be modeled as Lambertian using the given  $R$ . This is a significant simplification in field work because of the difficulty of measuring the full BRDF, and in radiative transfer calculations because of the additional computations required for non-Lambertian BRDFs.

However, when measuring  $R = E_u/E_d$  using irradiance sensors located some distance above the bottom, care is needed when ascribing the measured  $R$  to the bottom itself because  $E_u$  and  $E_d$  change throughout the water column. We therefore next consider the effects of the water between the bottom and the instruments, which are located a height  $h$  above the bottom. The depth dependence of  $R$  within the water column can be described via a diffuse attenuation coefficient for  $R$ , defined as

$$K_R = -\frac{d \ln R}{dz} = -\frac{d \ln(E_u/E_d)}{dz} = K_u - K_d$$

Here we have used the customary definitions of diffuse attenuation coefficients for upwelling ( $K_u$ ) and downwelling ( $K_d$ ) plane irradiances. In optically shallow waters,  $K_u$  will

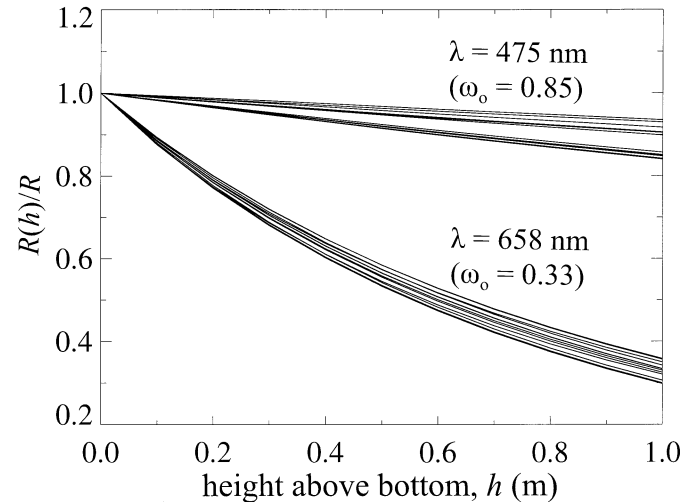


Fig. 8. Dependence of irradiance reflectance  $R$  on height above the bottom for two different sets of water IOPs (as labeled). The lines are for various BRDFs and solar angles. The water depth is 3 m.

be dominated by bottom-reflected light, but we can still expect that  $K_d$ , and thus  $K_R$ , will be strongly influenced by water-column absorption.

Figure 8 shows the variation in  $R$  with distance above the bottom for simulations with a water depth of 3 m. These simulations are for all BRDFs, both sets of IOPs (now using the actual  $a$  and  $b$  values at 475 nm [ $\omega_0 = 0.85$ ] and 658 nm [ $\omega_0 = 0.33$ ] cited above for LSI waters), and solar zenith angles of 0 and 88°. The curves fall into two distinct groups defined by the highly absorbing and highly scattering  $\omega_0$  values, with minor variability for the different solar angles and BRDFs. For the IOPs at 475 nm, measuring the bottom reflectance with instruments located as much as  $h = 60$  cm above the bottom would give an  $R(h)$  value that is within 10% of the  $R$  at the bottom itself. However, at 658 nm, where the water is highly absorbing, placing the instruments even 10 cm above the bottom would give an error of over 10% in the estimate of the bottom  $R$ ; at  $h = 60$  cm,  $R(h)$  is roughly one half of  $R$ . Thus, a wavelength-dependent correction would have to be made in order to determine  $R(\lambda)$  of the bottom from a measurement of  $R(h, \lambda)$ . This correction factor will depend strongly on the water IOPs and height above the bottom and must be computed anew for each water body.

However, the difficulty of correctly deducing the true bottom reflectance  $R$  from above-bottom irradiance measurements does not preclude the use of such measurements in modeling the bottom boundary as a Lambertian surface with the measured  $R$ . In radiative transfer simulations, the assumed Lambertian bottom of the water column can be placed at the depth of the instruments, i.e., at a distance  $h$  above the physical bottom. The measured  $R$  then incorporates the effects of both reflectance from the physical bottom and the effects of the water column between the instruments and the physical bottom. The light field computed in the water above the instruments will then be consistent with the measured  $R$  at the instrument location, to the extent that the upwelling radiance at height  $h$  above the actual bottom is isotropic (as

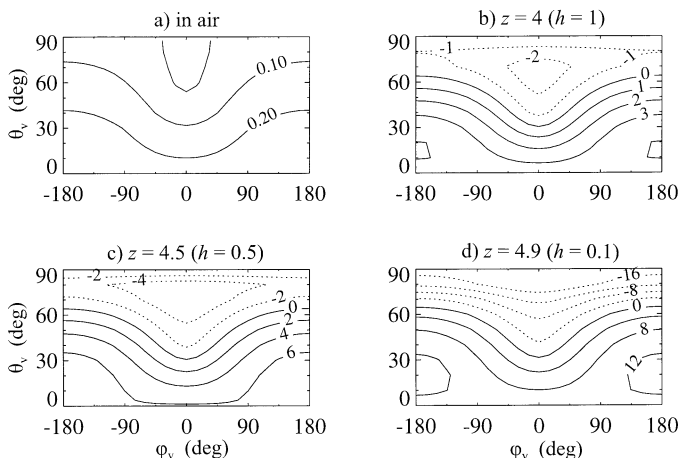


Fig. 9. Contours of the percentage error in the upwelling radiance  $L_u(\theta_v, \varphi_v)$  caused by replacing the conifer non-Lambertian BRDFs with a Lambertian BRDFs having the same irradiance reflectance. The bottom is at  $z = 5$  m, the solar zenith angle is  $\theta_s = 60^\circ$ , and the water IOPs are for 475 nm. Panels are labeled by the depth  $z$  (in meters) in the water column and by the equivalent height  $h$  above the bottom.

it would be for a Lambertian bottom placed at  $h$ ). The only error in the computed radiance will be due to the assumption of a Lambertian surface at level  $h$ , when in reality the upwelling radiance in the water column at level  $h$  is not Lambertian, even if the bottom itself is.

### In-water radiances

We have seen that a Lambertian BRDF can be substituted for a non-Lambertian BRDF with errors of order 10% in radiative transfer simulations related to PHILLS above-surface remote sensing. We next consider whether the same is true for in-water radiances, especially very near the bottom. Figure 9 shows a simulation of upwelling radiances for a water depth of 5 m, solar zenith angle of  $60^\circ$ , LSI IOPs at 475 nm, and the coniferous forest BRDF. Panel a shows the errors in the water-leaving radiance, and therefore corresponds to the plots of Figs. 5 and 6. Panels b to d show the errors in the in-water upwelling radiance at depths of  $z = 4$ , 4.5, and 4.9 m, which are respectively  $h = 1$ , 0.5, and 0.1 m above the bottom. In these three panels the viewing direction  $(\theta_v, \varphi_v)$  is the same as the reflectance direction  $(\theta_r, \varphi_r)$ , since there are no sea-surface refraction effects.

Half a meter above the bottom, the error is less than 8%. Even at 10 cm above the bottom, the maximum error, which occurs as grazing angles ( $\theta_v$  near  $90^\circ$ ), is less than 20%. Moreover, this error is more likely to be an artifact of the behavior of the idealized conifer BRDF model, which becomes infinite at  $\theta_v = 90^\circ$ , than a feature of actual vegetation BRDFs. The ooid sand BRDF used in Figs. 2 and 5 remains finite at  $\theta_v = 90^\circ$ , and the corresponding error at  $h = 10$  cm is less than 8% (0.5% in air). These errors increase if the bottom depth is very shallow. For example, if the bottom is at 1 m, then the errors 10 cm above the bottom are as large

as 60% at grazing angles for the conifer BRDF (and the in-air errors are  $\pm 5\%$ ). For the sand BRDF, the corresponding errors are less than 15% at  $h = 10$  cm (6% in air) in 1 m of water. In any case, it is difficult to envision situations of practical oceanographic interest involving the nearly horizontal radiances 10 cm above the bottom.

There is, however, one situation for which the substitution of a Lambertian BRDF for the actual non-Lambertian BRDF may cause large errors. In an active optical imaging system the instrument sends out a beam of light, which is reflected from the bottom and then received by a sensor colocated (or nearly so) with the source. In this geometry, one is always observing the hot spot. Thus the bottom may reflect a factor of two or more radiance, especially for slant-path lines of sight (large  $\theta$  values), more than would be expected if the bottom were Lambertian with the same  $R$ . In performance evaluation and data interpretation for such systems, the non-Lambertian benthic BRDF must be measured and included in radiative transfer calculations.

### References

- CABOT, F., AND G. DEDIEU. 1997. Surface albedo from space: Coupling bidirectional models and remotely sensed measurements. *J. Geophys. Res.* **102**: 19645–19663.
- DAVIS, AND OTHERS. 2002. Ocean PHILLS hyperspectral imager: Design, characterization, and calibration. *Opt. Express* **10**: 210–221.
- GORDON, H. R., AND O. B. BROWN. 1974. Influence of Bottom depth and albedo on the diffuse reflectance of a flat homogeneous ocean. *Appl. Opt.* **13**: 2153–2159.
- HAPKE, B. 1993. *Theory of reflectance and emittance spectroscopy*. Cambridge Univ. Press.
- HARRISON, A. W., AND C. A. COOMBS. 1988. Angular distribution of clear sky short wavelength radiance. *Solar Energy* **40**: 57–63.
- LEE, Z., K. L. CARDER, C. D. MOBLEY, R. G. STEWARD, AND J. S. PATCH. 1998. Hyperspectral remote sensing for shallow waters. I. A semianalytical model. *Appl. Opt.* **37**: 6329–6338.
- LYZENGA, D. R. 1978. Passive remote sensing techniques for mapping water depth and bottom features. *Appl. Opt.* **17**: 379–383.
- MARITORENA, S., A. MOREL, AND B. GENTILI. 1994. Diffuse reflectance of oceanic shallow waters: Influence of water depth and bottom albedo. *Limnol. Oceanogr.* **39**: 1689–1703.
- MAZEL, C. H. 1997. Diver-operated instrument for in situ measurement of spectral fluorescence and reflectance of benthic marine organisms and substrates. *Opt. Eng.* **36**: 2612–2617.
- MOBLEY, C. D. 1994. *Light and water: Radiative transfer in natural waters*. Academic.
- , AND OTHERS. 1993. Comparison of numerical models for computing underwater light fields. *Appl. Opt.* **32**: 7484–7504.
- , AND L. K. SUNDMAN. 2003. Effects of optically shallow bottoms on upwelling radiances: Inhomogeneous and sloping bottoms. *Limnol. Oceanogr.* **48**: 329–336.
- MODEST, M. F. 1993. *Radiative heat transfer*. McGraw-Hill.
- NICODEMUS, F. E., J. C. RICHMOND, J. J. HSIA, I. W. GINSBURG, AND T. LIMPERS. 1977. *Geometrical considerations and nomenclature for reflectance*. NBS Monograph 160, National Bureau of Standards.
- PHILPOT, W. D. 1989. Bathymetric mapping with passive multi-spectral imagery. *Appl. Opt.* **28**: 1569–1578.
- RAHMAN, H., B. PINTY, AND M. M. VERSTRAETE. 1993. Coupled

surface-atmosphere reflectance (CSAR) model 2. Semiempirical surface model usable with NOAA Advanced Very High Resolution Radiometer Data. *J. Geophys. Res.* **98**: 20791–20801.

VOSS, K. J., A. CHAPIN, M. MONTI, AND H. ZHANG. 2000. Instrument to measure the bidirectional reflectance distribution function of surfaces. *Appl. Opt.* **39**: 6197–6206.

ZHANG, H., K. J. VOSS, R. P. REID, AND E. LOUCHARD. 2003. Bi-

directional reflectance measurements of sediments in the vicinity of Lee Stocking Island, Bahamas. *Limnol. Oceanogr.* **48**: 380–389.

*Received: 27 September 2001*

*Accepted: 8 April 2002*

*Amended: 17 April 2002*